Available online at www.sciencedirect.com
ScienceDirect
Journal of Marine Systems 74 (2008) 120–133
JOURNAL OF MARINE SYSTEMS
www.elsevier.com/locate/jmarsys

# Vertical structure of tidal currents over Espartel and Camarinal sills, Strait of Gibraltar

A. Sánchez-Román [a,*], F. Criado-Aldeanueva [a], J. García-Lafuente [a], J.C. Sánchez [a,b]

[a] Departamento de Física Aplicada II, Universidad de Málaga, Málaga, Spain
[b] Grupo de Puertos y Costas, Universidad de Granada, Granada, Spain

Received 23 July 2007; received in revised form 7 November 2007; accepted 19 November 2007
Available online 5 February 2008

**Abstract**

ADCP velocity data collected in the two main sills of the Strait of Gibraltar (Camarinal and Espartel sills) have been used for analysing the vertical structure of main tidal constituents ($M_2$, $S_2$, $O_1$ and $K_1$) currents in this area. Two different periods (winter and summer) were considered in correspondence to seasonal variations in density profiles. Amplitudes and phases of the various tidal constituents have been compared for both periods and locations. Barotropic and baroclinic parts of the tidal currents have been extracted using the dynamical mode decomposition technique and the relative importance of each mode has been established in terms on the energy associated. In Espartel sill, the barotropic mode is more energetic in wintertime for all constituents except for $K_1$. Baroclinic modes have smaller contribution to total energy. Second and third baroclinic modes tend to be more energetic than the first one, especially during winter, this indicating a relatively complex vertical structure of the tidal currents. Over Camarinal sill, barotropic mode accounts for more than 90% of total energy in all the tidal constituents, the highest value (97%) observed for $M_2$.


*Keywords:* Tidal currents; Dynamical mode decomposition; Harmonic analysis; Seasonal variations; Velocity profilers; Strait of Gibraltar

## 1. Introduction

The Strait of Gibraltar connects the Mediterranean Sea and the Atlantic Ocean through a rather complicated system of sills and narrows. It has a length of nearly 60 km and a mean width of 20 km. Its shallower depth, less than 300 m, is found in the main sill of Camarinal, CS (west of Tarifa) and its minimum width of around 14 km coincides with the contraction of Tarifa Narrows (see Fig. 1). The Strait is the scenario of a well-studied baroclinic exchange between two basins with different densities. The net loss of freshwater in the Mediterranean Sea, due to the excess of evaporation over precipitation and river runoff, represents the main driving force of the circulation through the Strait, which is inverse estuarine with two counter flowing currents: in the upper layer warm and relatively fresh Atlantic water ($S_A \sim 36.2$) flows eastward, spreads into the Mediterranean Sea and is ultimately transformed in colder and saltier ($S_M \sim 38.5$) water that flows westward as an undercurrent. The influence of this extends far away from the strait in the Atlantic ocean (Reid, 1979; Lacombe and Richez, 1982).

* Corresponding author. Dpto. Física Aplicada II, E.T.S.I. Informática, Campus de Teatinos, Universidad de Málaga, 29071 Málaga, Spain. Tel.: +34 952 132849; fax: +34 952 131355.
*E-mail address:* Antonio.sanchez@ctima.uma.es (A. Sánchez-Román).

0924-7963/$ - see front matter © 2008 Published by Elsevier B.V.
doi:10.1016/j.jmarsys.2007.11.007

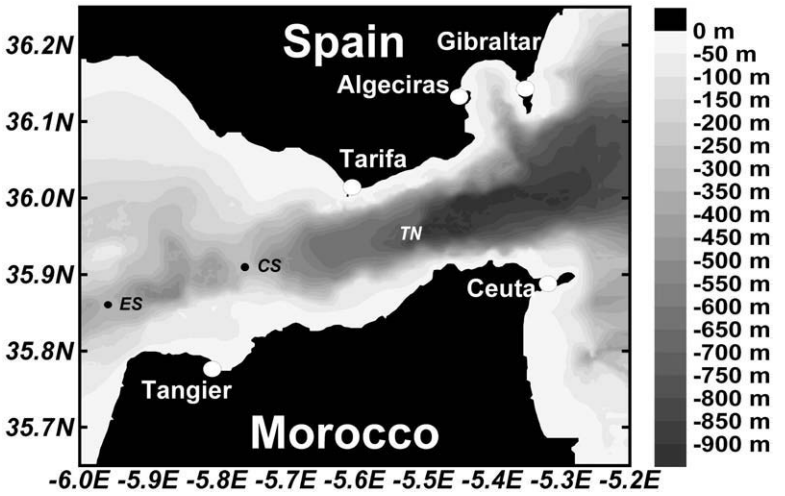


Fig. 1. Map of the Strait of Gibraltar showing the main topographic features. TN corresponds to the minimum width section of Tarifa narrows. ES and CS indicates the locations of the sills of Camarinal and Espartel, respectively, and also the mooring lines location of the observed data.

The mean flow through the Strait of Gibraltar is modified by various processes at different time scales. It shows seasonal (Garrett et al., 1990; García Lafuente et al., 2002a) and inter-annual variability, sub-inertial (*O* (10 days)) modifications driven by winds and, mainly, by atmospheric pressure differences between the Atlantic ocean and Mediterranean Sea (Candela et al., 1989; García Lafuente et al., 2002b) and diurnal and semidiurnal variations due to strong tidal currents. The topographic interaction of tidal flow with CS gives rise to either internal hydraulic jumps (Armi and Farmer, 1988) or arrested topographic waves (Bruno et al., 2002) which are eventually released as internal bores progressing towards the Mediterranean Sea with a train of energetic internal waves on its wake (Richez, 1994). They occupy the high frequency range and, along with the strong tidal flow, are the most noticeable hydrodynamic feature of the area.

The tidal signal in the Strait has been extensively studied and analysed in the past. García Lafuente et al. (1990) described the structure of the barotropic (vertical) tide in the Strait and Candela et al. (1990) extended the analysis of the barotropic tide to $M_2$ tidal currents. The vertical tide behaves basically as a standing wave with amplitudes increasing towards the Atlantic Ocean (García Lafuente et al., 1990). At the semidiurnal frequency, the pressure gradient along the strait is mainly balanced by the acceleration of the flow, while the cross-strait momentum balance appears to be mostly geostrophic (Candela et al., 1990). At this frequency, there is also a strong correlation between the depth of the interface and the strength of the tidal currents.

The tidal transport through the Strait was studied by Bryden et al. (1994) and García Lafuente et al. (2000). Bruno et al. (2000) have described the vertical structure of the semidiurnal tide at CS and, in accordance with previous estimations (Candela et al., 1989; Mañanes et al., 1998), have reported that the semidiurnal variance at CS is mainly due to the barotropic mode, with less than 10% accounted by baroclinic modes. Tsimplis (2000) has performed a similar analysis in CS by means of 100 days (18/01/97–29/04/97) series of ADCP data registered with a vertical resolution of 8 m every 30 min. Wang (1993) studied the tidal flows, internal tide and fortnightly modulation by mean of a numerical model and Tsimplis and Bryden (2000) have estimated the water transports through the strait; García Lafuente et al. (2000) have analysed the tide in the eastern section of the strait and Baschek et al. (2001) have estimated the transport with a tidal inverse model. Recently, Sannino et al. (2002, 2004) have implemented a numerical model for analysing the mean exchange through the Strait and the semidiurnal tidal exchange respectively. In contrast to CS, there are no studies on the vertical structure of tidal currents over Espartel sill (ES), which also plays an important role in the exchange as it represents the westernmost shallow constraint before the Mediterranean flow sinks into the Gulf of Cadiz. This work describes the vertical profile of the main diurnal ($O_1$ and $K_1$) and semidiurnal ($M_2$ and $S_2$) tidal constituents at ES from observed data in two different periods of the year. For comparison purposes, winter data from CS have also been analysed.

Tidal velocities can be separated into barotropic and baroclinic components by employing either empirical

orthogonal function (EOF) decomposition (Kundu et al., 1975; Candela et al., 1990; Mañanes et al., 1998; Bruno et al., 2000) or a dynamical mode decomposition, DMD (Marchuk and Kagan, 1970; Kundu et al., 1975; Schott, 1977; Siedler and Paul, 1991; Müller and Siedler, 1992; Bruno et al., 2000, Tsimplis, 2000). In the EOF decomposition, the resulting EOFs are solely determined by the statistics of the data in use. The eigenfunctions, therefore, are sometimes difficult to interpret in terms of their physical origin. In addition, this decomposition allows barotropic and baroclinic components of the tidal velocity to be separated only if they are orthogonal; otherwise, their separation with different temporal weights is impossible even when high vertical resolution data are available (such as data collected by Acoustic Doppler Current Profilers, ADCP). With DMD, a set of vertical dynamical modes of pressure (or another flow variable) is obtained from the hydrodynamic equations for given density profiles. A least-square estimation procedure is then used to determine the modal amplitudes and phases from the observed values of tidal velocities at different depths. In this work, the decomposition through DMD, which makes use of physical constraints, has been preferred.

The paper is organized as follows: Section 2 describes the data set and methodology. In Section 3, the main results on vertical structure of tidal currents over ES and CS are presented and discussed. Dynamical mode decomposition (DMD) results are also interpreted. Finally, Section 4 summarises the conclusions.

## 2. Data and methods

### 2.1. ADCP data

ADCP data were collected in the two main sills of the Strait of Gibraltar (ES and CS, see Fig. 1) at its western approach. The ES data comes from a monitoring station located at 35° 51.70′N, 05° 58.60′W installed in September 2004. It consists of an up-looking moored ADCP at 340 m depth (20 m above the seafloor) that resolves 40 bins, 8-meter thick each one, and provided horizontal velocity at 40 levels every 30 min. The upper 30 or 40 m of the water column were missed. This work analyses the data collected in 2005.

CS data come from a monitoring station installed at 35° 54.80′N, 05° 44.70′W within the frame of a special programme of Woods Hole Oceanographic Institution. The station consisted of an up-looking mooring ADCP that measured the water column velocity between 54 and 274 m depth with sampling interval of 60 min. The bin-size of the ADCP was 10 m and 23 bins were resolved. The time series in this sill spans from October 1995 to April 1996, covering the winter season.

### 2.2. CTD data

MEDATLAS database provided historical Conductivity–Temperature–Depth (CTD) profiles in the area of CS and ES in order to determine mean density profiles in these points. The area within 35° 53.6′N–35° 55.1′N/05° 43.1′W–05° 45.3′W has been considered to be representative for CS and the area within 35° 48.6′N–35° 53.9′N/05° 56.7′W–06° 00.8′W, for ES. 40 and 48 CTD profiles have been identified for each area, respectively, most of them from the field work carried out during the Gibraltar Experiment (1986).

In order to account for seasonal variations of the density profiles, two representative periods have been selected: “winter” period corresponds to profiles between 01/02 and 30/04 and “summer period” corresponds to profiles between 01/06 and 31/10 (see Section 3.6 for details). Although they do not exactly correspond to winter and summer months, we will refer to them as winter and summer periods, respectively. This selection relies on the vertical density stratification of the upper layer of the water column. From February to April, there is no signature of the seasonal thermocline that develops in summertime, whereas from June to October it is clearly established. The other months have been considered as transition periods, since they share characteristics of both periods and are not likely to be representative of a typical winter or summer pattern.

## 3. Results and discussion

### 3.1. Mean along-strait currents

Similarly to the CTD data, velocity series have been divided into winter and summer periods according to the criterion of Section 2. The vertical structure of the mean currents at ES showing the two-layer character of the flow is displayed in Figs. 2A–B. The upper layer flows towards the Mediterranean Sea with a velocity of 25–30 cm $s^{-1}$ above 120–130 m that diminishes to zero at 190 m (the mean depth of the interface). Below this depth, the water flows towards the Atlantic with gradually increasing velocity until about 270 m, where a maximum value of ~130 cm $s^{-1}$ is reached. From this depth downwards, velocity decreases. Direction remains almost constant in the upper and lower layers (within 9°). There are slight differences between the winter and summer profiles: in summertime, velocity in the upper layer remains nearly constant until ~150 m, then decreasing to zero, whereas in

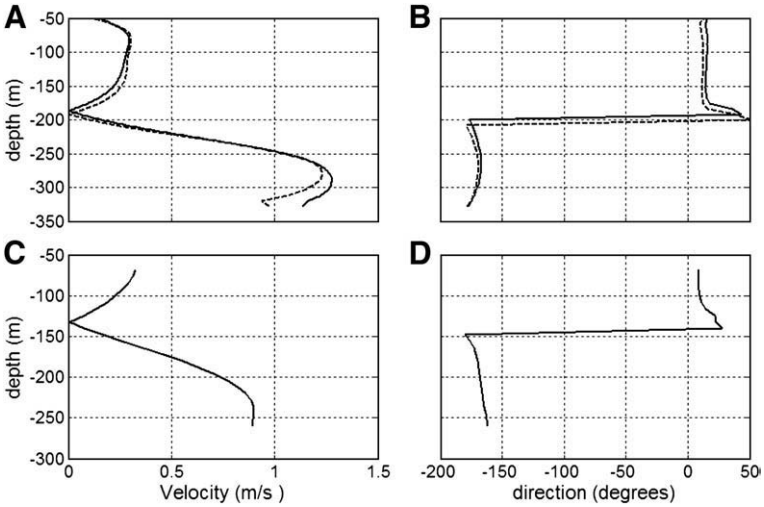


Fig. 2. Mean vertical profiles for the two mooring line locations: mean absolute along-strait velocity in (A) ES (solid line for winter time; dashed line for summer time); and (C) CS. Direction (anticlock-gyre from East) is also shown in (B) for ES (solid line for winter time; dashed line for summer time) and (D) for CS.

wintertime, the decreasing starts at around 100 m. Null velocity surface is around 10 m shallower in winter than in summer and maximum lower layer velocity is higher and is found deeper in winter.

The vertical structure of mean currents in CS during winter is displayed in Fig. 2C–D. As expected, the zero velocity surface is shallower (around 135 m depth) and the outflowing velocity is less than in ES. Even so, the maximum velocity observed here is 15% higher than that reported by Tsimplis (2000) for the period 01/97–04/97. Discrepancies are probably due to inter-annual variations since the data analysed here (02/96–04/96) corresponds to a different year, although instrumental considerations cannot be disregarded at all. Similar to ES, direction remains almost constant (within 11°) in the upper and lower layers. It is interesting to notice the spatial acceleration of the outflow from CS to ES, which is consequence of the progressive diminution of the outflow cross-section towards the west.

### 3.2. Tidal ellipses

ADCP time series were subjected to the standard harmonic analysis (Foreman, 1978; Pawlowicz et al., 2002) to obtain the tidal ellipses of the main semidiurnal ($M_2$, $S_2$) and diurnal ($O_1$, $K_1$) tidal constituents in ES and CS. They exhibit the highest amplitudes and also turn out to be the most stable in terms of signal/noise ratio (snr). Therefore, they are the most suitable to describe the tidal flow at these frequencies.

The tidal ellipses at selected depths, displayed in Fig. 3, show the high polarization of the flow along the axis of the Strait. The minor semi-axis is always less than 15% of the major one, in agreement with previous results by Tsimplis (2000) and Mañanes et al. (1998). The percentage decreases towards the sea surface. The highly rectilinear tidal flow justifies the use of the along-strait velocity component to accomplish a scalar analysis of the tidal currents. For this reason, ADCP velocity was rotated 17° anticlockwise to obtain the along-strait velocity and the scalar harmonic analysis of this component has been performed to calculate amplitude and phase of tidal constituents.

### 3.3. Harmonic analysis

#### 3.3.1. Semidiurnal constituents

The vertical pattern of the along-strait velocity of $M_2$ and $S_2$ in ES is shown in Fig. 4. The amplitude of $M_2$ (panel A) reaches a maximum of ~58 cm $s^{-1}$ at ~240 m, 50 m below the mean depth of the interface, inside of the Mediterranean layer (Fig. 3A). Then, the amplitude decreases quickly towards the bottom. Only slight variations between winter and summer periods are found, one of them being the relative minimum of ~47 cm $s^{-1}$ at 190 m observed in summertime that is not evident in winter. Amplitude of $S_2$ (panel C) remains almost constant at ~16 cm $s^{-1}$ for summertime until ~240 m, where it starts decreasing with depth. In wintertime, the amplitude slowly increases from

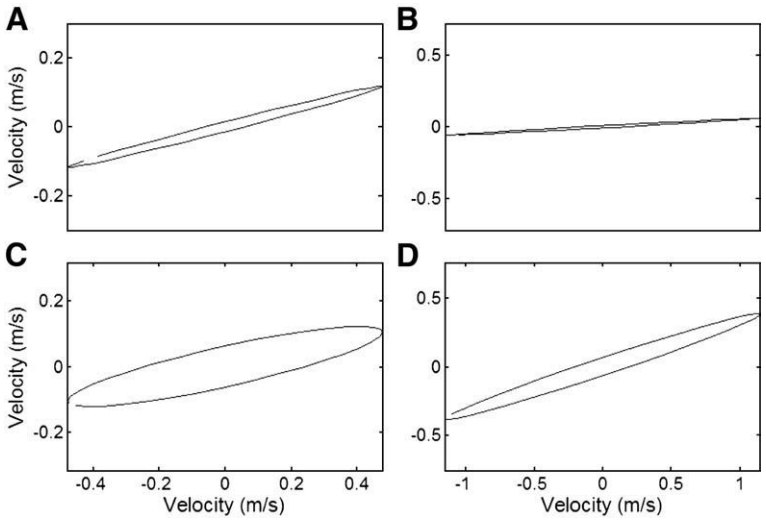


Fig. 3. $M_2$ tidal constituent ellipses at 96 m (panel A) and 256 m (panel C) at ES and at 56 m (panel B) and 194 m (panel D) at CS. Relative importance of both semi-axis is clearly evidenced.

~18 cm $s^{-1}$ near the surface until ~26 cm $s^{-1}$ at ~220 m, then decreasing with depth. Discrepancies between both periods are evident, with winter values 30% higher on average and up to 50% higher at ~220 m, level of the maximum difference.

The phase of $M_2$ is maximum nearly, but slightly above, the depth of the maximum amplitude. It is more pronounced in summer, a fact that could be related to the different stratification of the upper water column. The dependence of the phase with depth implies downwards phase propagation above the depth of local maximum and upwards propagation below it. According to the linear theory of internal waves in a continuously stratified flow, the group velocity (that is, the energy) has a vertical propagation of different sign that phase, that is upwards (downwards) from the depth of maximum phase, which means a local divergence of energy towards the surface and the bottom. The maximum of $M_2$ amplitude found below this depth as well as the secondary local maximum around 150 m above this depth could be related to this vertical energy propagation.

$S_2$ constituent shows a similar vertical pattern, although the relative position in the water column of the amplitude and phase maxima in winter is different from the pattern of $M_2$ and also from that of $S_2$ in summer. The nearly constant phase difference of 30° between $S_2$ and $M_2$ ($S_2$ leading $M_2$) indicates an age of the tide of 1.2 days, that is, spring tide happens one day later than new or full moon. The increase of $S_2$ phase near the bottom implies greater age of the tide in this area. The greater $S_2$ amplitude in winter implies stronger (weaker) spring (neap) tides in this season, a feature enhanced between 170 and 230 m (around the depth of the mean interface) because of the increase of $M_2$ amplitude within this depth range in winter.

However, following the Rayleigh criterion, the length of the time series does not allow a satisfactory resolution of the $S_2$–$K_2$ constituents couples, which demands a record length of at least six months. For this reason, $S_2$ estimations may be affected by its non-resolved companion and part of the differences in amplitude and phase between summer and winter could be explained by this coupling. To further investigate this topic, a 1-year (2005) tidal harmonic analysis has been performed to obtain the amplitude rate and phase difference between both constituents that will lead to infer the $S_2$–$K_2$ coupling and isolate the $S_2$ contribution. As a result, variations of $S_2$ amplitude is reduced ~50% but coupling between constituents do not significantly account for $S_2$ phase which is more likely related to seasonal variability.

The amplitude of $M_2$ in CS slightly increases from the first bins to ~175 m depth (40 m below the mean depth of the interface, Fig. 5), where a maximum over 120 cm $s^{-1}$ is reached. The maximum is shallower and more than twice greater than in ES. Below 175 m, the amplitude decreases moderately. This pattern agrees with that of Tsimplis (2000) from mid-January to April and of Candela et al. (1990) spanning different periods. $S_2$ amplitude remains almost constant at ~50 cm $s^{-1}$ until ~150 m, then gradually decreasing with depth. The values are again greater than in ES.

The phase of $M_2$ in CS is maximum some tens of meters below the surface of zero mean velocity, at around 175 m, the same depth in which the amplitude

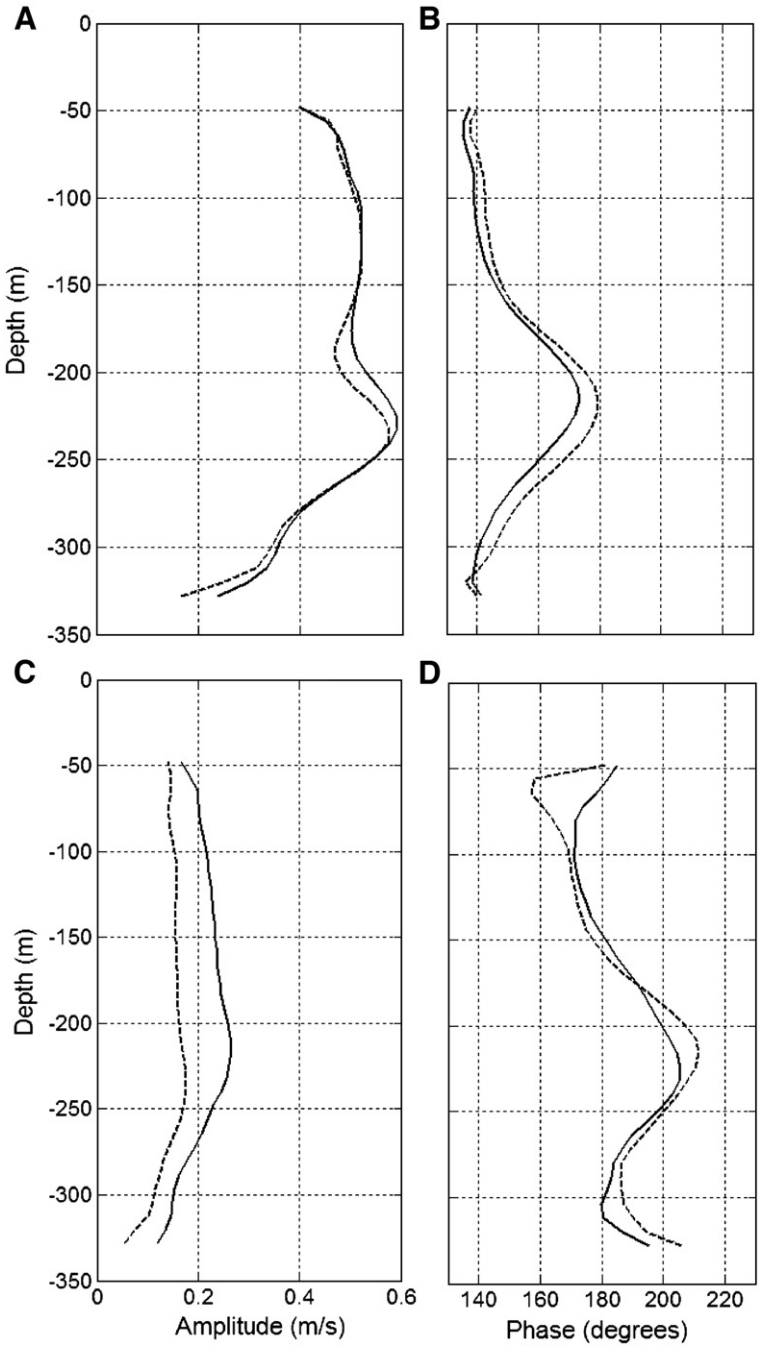


Fig. 4. Vertical structure of the semidiurnal tidal constituents $M_2$ (amplitude, panel A; phase panel B) and $S_2$ (amplitude panel C; phase panel D) both for winter (solid line) and summer (dashed line) periods at ES.

also reaches maximum. It is less pronounced than in ES and, as in this place, it implies phase propagation from above and below and, therefore, energy divergence upwards and downwards from this depth. Phase of $S_2$ is greater than phase of $M_2$ above 160 m in the upper layer but it is less or equal in the Mediterranean layer. It is interesting to emphasise the good agreement of these results and those reported by Tsimplis (2000) with data of the same season but different year. According to the values in Fig. 5B, spring tides in CS delay 0.5 to 1 day

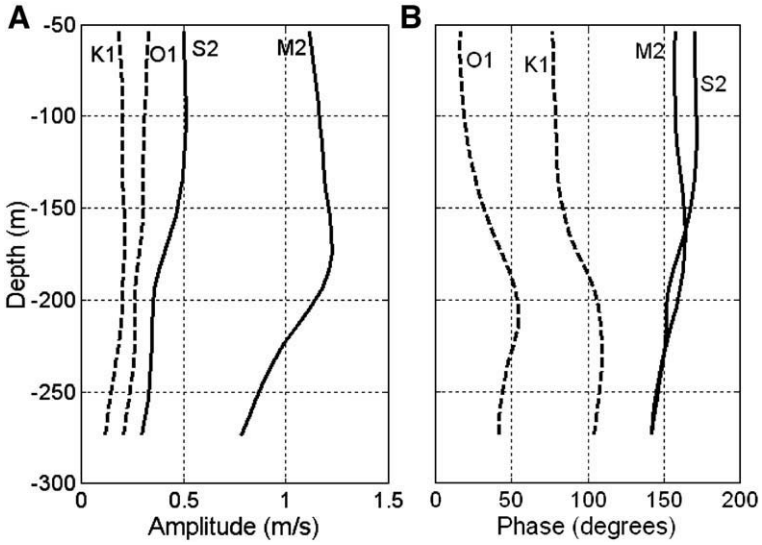


Fig. 5. Vertical structure (amplitude, panel A; phase, panel B) of the main semidiurnal (solid line) and diurnal (dashed line) tidal constituents for winter period at CS.

the new/full moon in the upper layer while they happen simultaneously with or even shortly before new/full moon in the lower layer. The diminution of $S_2$ phase in the Mediterranean layer in CS contrasts with the increase in ES, where it reaches a noticeably relative maximum well below the interface (Fig. 4D). The depth averaged phase of $M_2$ in CS (156°) is quite similar to that in ES (150°) while the depth averaged phase of $S_2$ in ES (186°) is greater than in CS (160°).

### 3.3.2. Diurnal constituents

The vertical distribution of $K_1$ and $O_1$ for winter and summer is shown in Fig. 6. Amplitude of $O_1$ (panel A) reaches a maximum of 25 cm $s^{-1}$ at 240 m, the same depth of $M_2$ maximum. There are no differences between summer and winter periods. In contrast, $K_1$ amplitude is 2 to 4 cm $s^{-1}$ greater in summer increasing to 6–7 cm $s^{-1}$ in the lower bins (panel C). Similarly to $O_1$, maximum value is observed at ~240 m in both periods. Phases of both constituents (Fig. 6B–D) exhibit a similar behaviour with maxima at ~230 m and ~220 m, respectively. The phase of $K_1$ in summer leads by ~8° the phase in winter until the lower bins, where they diverge. Similarly to what happened to the $S_2$ constituent, $K_1$–$P_1$ coupling must be considered as a possible source of seasonal variability. The procedure described for the $S_2$ constituent has also been performed to isolate the $K_1$ contribution. In contrast to $S_2$, the coupling explains ~50% of the phase discrepancies but does not significantly affect the amplitude behaviour, which is more likely related to seasonal variability.

Amplitude of diurnal constituents is nearly depth-independent in CS (Fig. 5). Rather constant values of ~30 cm $s^{-1}$ ($O_1$) and ~20 cm $s^{-1}$ ($K_1$) remains until ~200 m, then decreasing slightly to the bottom. The values are somewhat higher than in ES and match reasonably well those reported by Tsimplis (2000). The vertical structure of the phases is very similar, with a rather constant difference of 50° and greater values in the lower layer that implies a delay in the occurrence of maximum diurnal tidal currents in this layer.

## 3.4. Stability of the tidal constituents

Following Tsimplis (2000), stability of the tidal constituents has been estimated by splitting all the data available for each location into fortnightly periods. The results of the harmonic analysis for each of them allows for the estimation of a mean value and a standard deviation for the amplitude and phase of each tidal constituent. The ratio std/mean of the amplitude of each constituent is the stability criterion used. When the standard deviation for a given constituent is as large as the mean amplitude, the reliability of the harmonic constants is very poor. Fig. 7 shows that the ratio is always below 0.4 in ES, where $S_2$ is the noisiest signal. In CS, the ratio is very low except for $K_1$ constituent. As a rule, the smaller the amplitude, the greater the ratio and, hence, the noisier the signals. The larger amplitudes in CS compared with those of ES imply less noisy signals in that place.

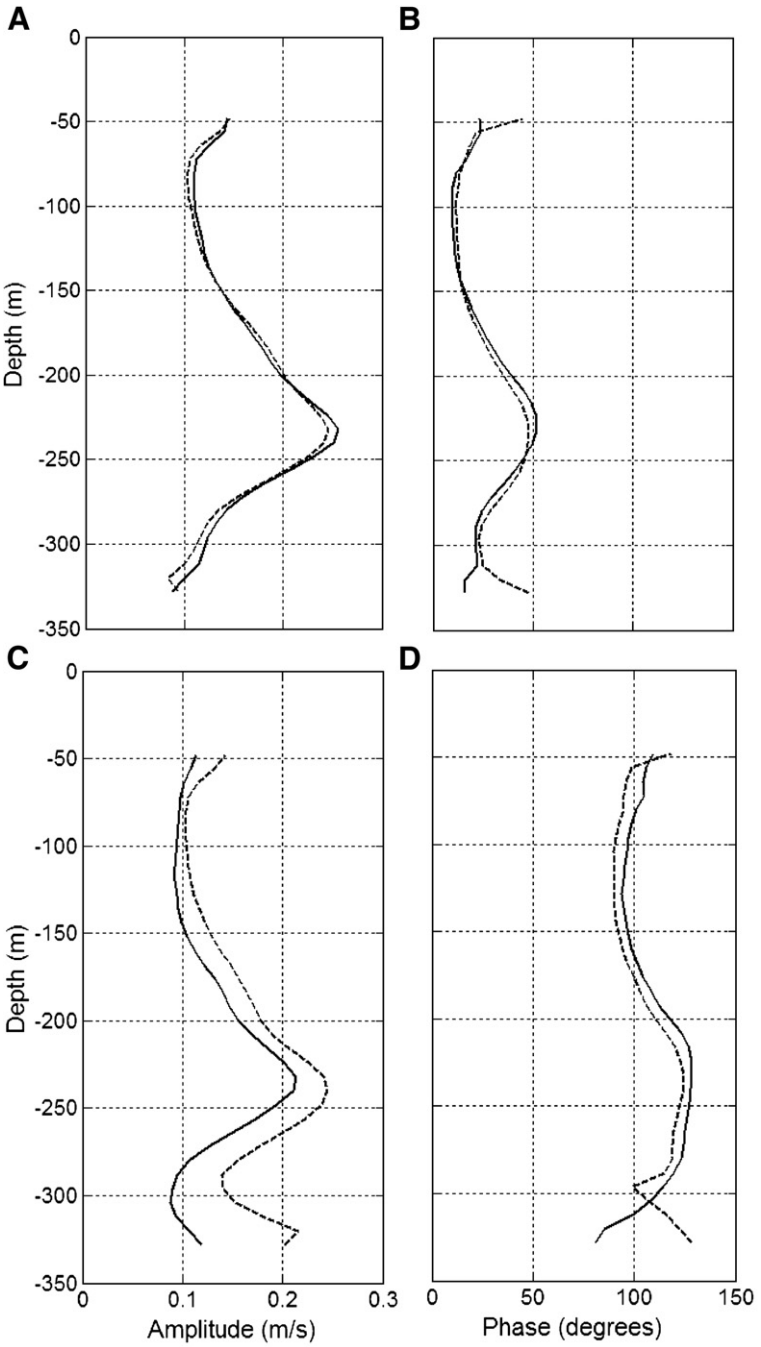


Fig. 6. Vertical structure of the diurnal tidal constituents $O_1$ (amplitude, panel A; phase panel B) and $K_1$ (amplitude panel C; phase panel D) both for winter (solid line) and summer (dashed line) periods at ES.

### 3.5. Normal mode decomposition

In order to separate tidal velocities into barotropic and baroclinic components, dynamical mode decomposition (DMD) technique has been used. DMD uses the linearized hydrodynamics equations with the Boussinesq approximation and the assumptions that dissipative and non-linear advective effects are negligible.

DMD assumes that the solutions in all variables can be expressed as the sum of various vertical orthogonal

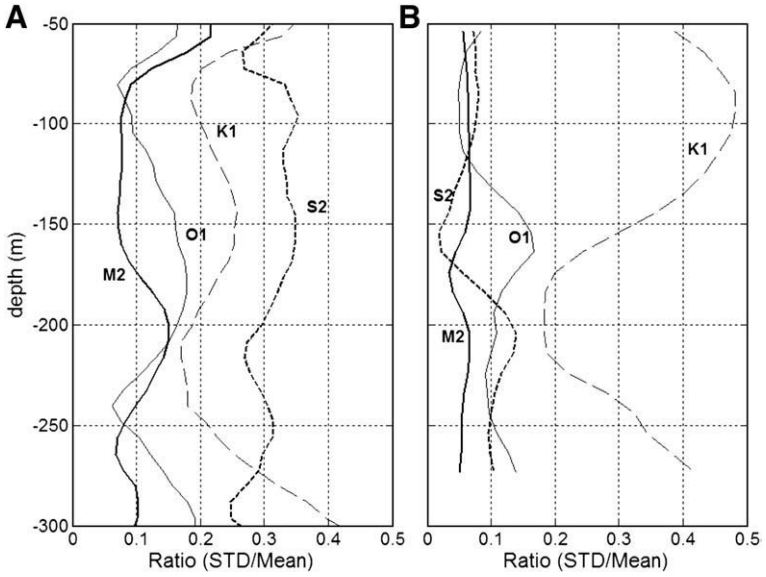


Fig. 7. Vertical distribution of the mean/std ratio for amplitude of each tidal velocity constituent ($M_2$, thick solid line; $S_2$, thick dashed line; $O_1$, thin solid line; $K_1$, thin dashed line) both for ES (panel A) and CS (panel B).

normal modes. The vertical structure of each mode is described by $\psi_n(z)$ and the solutions of the velocity components ($u$, $v$, $w$) and pressure and density perturbations ($p$, $\rho$) are then written in the form:

$$w(x,y,z,t) = \sum_{n=0}^{\infty} w_n(x,y,t)\psi_n(z) \tag{1}$$

$$\{u(x,y,z,t), v(x,y,z,t), p(x,y,z,t)/\rho_0\} = \sum_{n=0}^{\infty} \{u_n(x,y,t), v_n(x,y,t), p_n(x,y,t)\} \frac{d\psi_n(z)}{dz} \tag{2}$$

$$\rho = (x,y,z,t) = \sum_{n=0}^{\infty} \rho_n(x,y,t) \frac{d^2\psi_n(z)}{dz^2}. \tag{3}$$

Using the orthogonality condition of the different modes (Birkhoff and Rota, 1962; Gill, 1982)

$$\int_{-H}^{0} N^2 \psi_n(z)\psi_m(z)dz = 0 \quad \text{if } m \neq n \tag{4}$$

and substituting Eqs. (1)–(3) into the equation of motion leads to the classical eigenvalue equation:

$$\frac{d^2\psi_n(z)}{dz^2} + \frac{N^2(z)}{c_n^2}\psi_n(z) = 0 \tag{5}$$

where $c_n$ is the phase speed of mode $n$ and $N^2$ is the buoyancy frequency. Eq. (5) is solved using boundary conditions of flat bottom ($w_{-H}=0$) and rigid lid free surface ($w_0=0$), which in terms of $\psi_n(z)$ are:

$$\psi_n(z) = 0 \qquad \text{for } z = 0 \text{ and } z = -H. \tag{6}$$

Eqs. (5)–(6) constitute a Sturm–Liouvuille problem for eigenvectors $\psi_n(z)$ with eigenvalues $1/c_n^2$.

### 3.6. Normal modes solutions for Espartel and Camarinal stratification

Fig. 8A shows the density profiles from MEDATLAS for all the stations selected for ES. In winter, the surface layer is rather homogeneous and density is nearly constant until ~150 m. In summer, a sub-surface pycnocline of thermal origin develops, but below 60 m depth the distribution of density is nearly independent of the time of the year. In CS, the density profiles selected from MEDATLAS correspond to winter (February–April, Fig. 8C). The vertical distribution is similar to that of ES for the same period with a rather homogeneous water column until ~100 m and a shallower pycnocline (interface) due to its easternmost location.

The $N(z)$ profiles are shown in Fig. 8B–D. The seasonal variation of density is evident in ES, where the winter profile has a sole peak at ~210 m whereas the summer profile also peaks at ~50 m. In CS, the maximum in Brunt–Vaisalla frequency is founded at ~140 m.

The solution of Eq. (5) using these $N(z)$ profiles with boundary conditions (Eq. (6)) provides the vertical shape

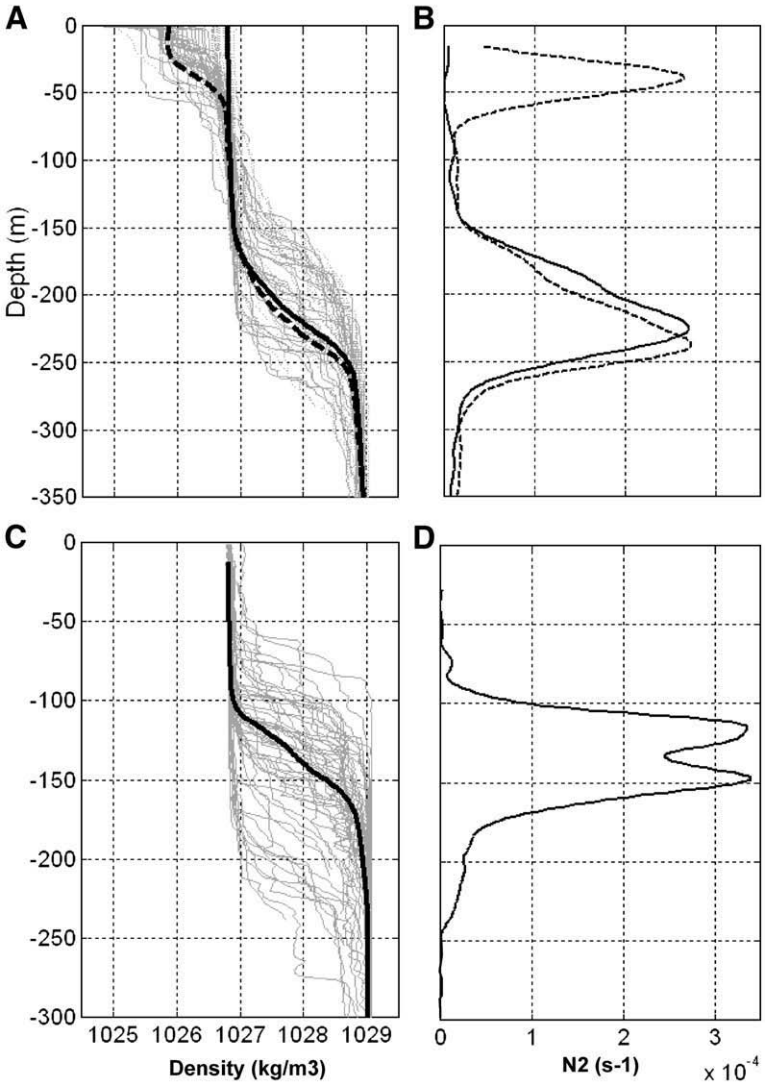


Fig. 8. A) Density profiles for all the stations selected for ES (thin grey lines). Mean density profile for winter (black solid line) and summer (black dashed line) periods have been superposed. B) Brunt–Vaisalla ($N^2$) mean profiles for winter (solid line) and summer (dashed line) periods at ES. C) Density profiles for all the stations selected for CS (thin grey lines). Mean density profile for winter period have been superposed. D) Brunt–Vaisalla ($N^2$) mean profile for wintertime at CS.

of the normal modes $\psi_n(z)$ for the vertical component of velocity. First derivative of $\psi_n(z)$ provides the vertical shape of the normal modes for the horizontal components $\varphi_n(z)$, according to Eq. (2). Fig. 9 shows the vertical shape of the first four baroclinic modes, $\varphi_n(z)$ ($n=1,\ldots, 4$) for winter (panel A) and summer (panel B) periods in ES and for winter in CS (panel C) normalised to maximum amplitude. However, the normalisation

$$\int_{-H}^{0} \varphi_n^2(z)dz = 1 \tag{7}$$

turns out to be more convenient and will be used henceforth as it allows for a direct interpretation of the relative importance of each mode in terms of the energy associated to it.

Let us consider along-strait tidal currents of the form:

$$u_l = a_l \cos(\omega t - \theta_l) \tag{8}$$

where $a_l$, $\theta_l$ ($l=1,2,\ldots, L$, number of bins sampled) are, respectively, the computed current amplitude and phase (harmonic constants) of the constituent of frequency $\omega$. The above expression can be written:

$$u_l = A_l \cos(\omega t) + B_l \sin(\omega t) \tag{9}$$

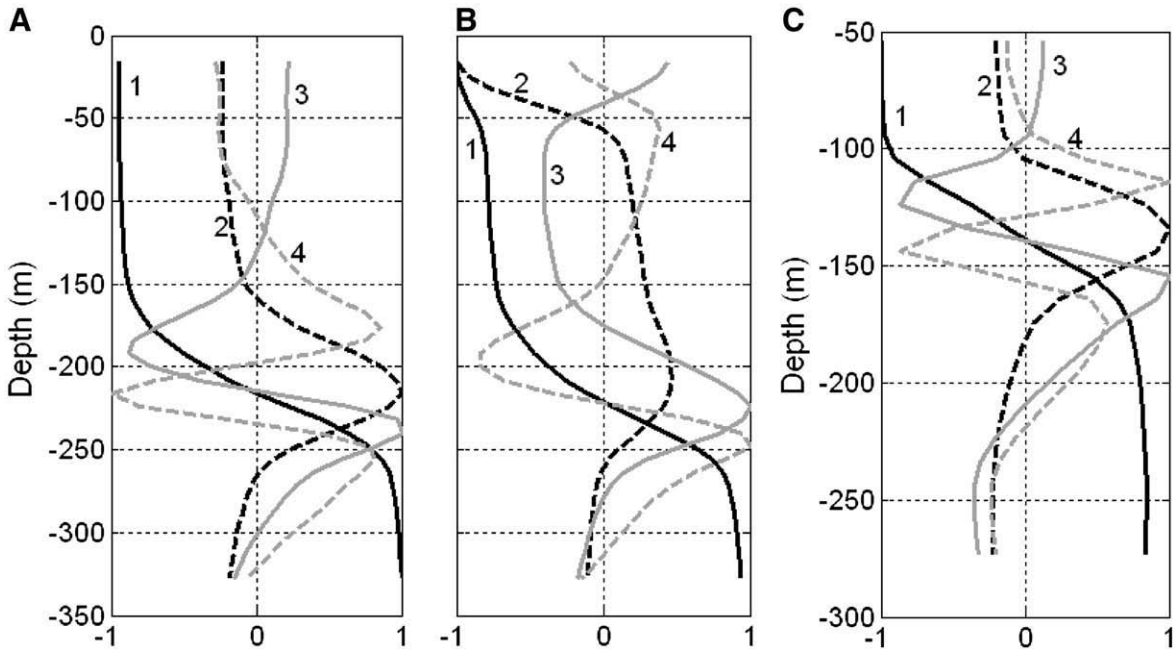


Fig. 9. First four baroclinic "horizontal" normal modes (#1, black solid line; #2, black dashed line; #3, grey solid line; #4, grey dashed line), $\varphi_n(z)$for winter (panel A) and summer (panel B) periods at ES and for wintertime at CS (panel C) normalised to maximum amplitude. An identificative number for each mode has also been labelled. Notice that this normalisation to maximum amplitude has only been used for this figure for a better visualisation of the vertical shape. For calculations the more convenient Eq. (7) is preferred.

with

$$A_l = a_l \cos\theta_l;\ B_l = a_l \sin\theta_l \tag{10}$$

The next step is to reproduce the coefficients $A_l$ and $B_l$ through a linear combination of the theoretical modes:

$$A_l = \sum_{n=1}^{K} C_n \cdot \varphi_n + \text{noise}; \tag{11}$$
$$B_l = \sum_{n=1}^{K} S_n \cdot \varphi_n + \text{noise}.$$

Coefficients $C_n$ and $S_n$ are determined by minimisation of the noise in Eq. (11) through least-squares fitting. The number of modes in the summation $K$ cannot exceed the number of bins $L$ and must be selected taking into account the number of degrees of freedom (NDF) in the fitting. Schott (1977) and Siedler and Paul (1991) recommended a minimum NDF of 11. The fitting was carried out using different NDF, the results being fairly insensitive to the NDF provided that it is greater than 11. Due to the negligible contribution of higher modes, $K$ was fixed to 10 so that NDF is 30 for ES and 13 for CS. The vertical structure of each mode is obtained through the products $(C_n,S_n)\cdot\varphi_n(z)$, where the coefficients are independent of depth. This vertical structure is often described in terms of amplitude $a_n$ and phase $\theta_n$ of each mode, computed according to

$$a_n^2 = C_n^2 + S_n^2;\quad \theta_n = \tan^{-1}\left(\frac{S_n}{C_n}\right). \tag{12}$$

Tables 1–3 summarise the results of the fitting. In all cases, the combination of the barotropic and the first five baroclinic modes (normalised to Eq. (7)) reproduces accurately the amplitude and phase profiles of the tidal constituents, as shown in Fig. 10 for semidiurnal constituents. Since ES data corresponds to summertime and CS data to wintertime, the fitting quality turns out to be rather insensitive to seasonal variations. Relative importance of each mode can be established in terms of the energy associated. Squaring Eq. (2) and then integrating between bottom and the surface, yields:

$$\int_{z=-H}^{z=0} u^2(x,y,z,t)dz = \sum_{n=0}^{\infty} u_n^2(x,y,t) \tag{13}$$
$$\times \int_{z=-H}^{z=0} \varphi_n^2(z)dz = \sum_{n=0}^{\infty} u_n^2(x,y,t)$$

where the normalisation (Eq. (7)) has been used. The LHS is proportional to kinetic energy associated to

Table 1
Amplitude $a_n$, phase $\theta_n$ and percentage of energy (inside parenthesis) for the barotropic mode and first five baroclinic modes normalised to Eq. (7) over ES during summer time

| | Constituent | | | |
|---|---|---|---|---|
| | $M_2$ | $S_2$ | $O_1$ | $K_1$ |
| Barotropic | 6.3, 152 (76.9) | 2.0, 186 (73.2) | 2.0, 36 (69.9) | 2.7, 117 (79.8) |
| Baroclinic 1 | 1.5, 154 (4.4) | 0.6, 141 (8.0) | 0.2, −62 (0.4) | 0.9, 134 (9.6) |
| Baroclinic 2 | 1.6, 171 (4.8) | 0.6, 221 (6.5) | 0.9, 11 (14.0) | 0.7, 253 (4.9) |
| Baroclinic 3 | 2.0, 223 (8.0) | 0.5, 239 (4.4) | 0.7, 72 (9.2) | 0.3, 181 (1.3) |
| Baroclinic 4 | 1.4, 152 (3.8) | 0.4, 163 (3.9) | 0.3, 30 (2.0) | 0.1, 170 (0.1) |
| Baroclinic 5 | 0.9, 169 (1.6) | 0.3, 169 (2.2) | 0.2, −39 (0.7) | 0.4, 141 (1.7) |

horizontal movement. The coefficients $u_n$ in Eq. (13) are the amplitudes $a_n$ computed from Eq. (12) and each term on the summation of the RHS, which in practice extends from $n=0$ to $n=K$, indicates the amount of energy accounted by each mode. The quotient:

$$E_n = \frac{a_n^2(x_A, y_A)}{\sum_{n=0}^{K} a_n^2(x_A, y_A)} \tag{14}$$

represents the fraction of total energy explained by mode $n$.

Results of these calculations are summarised in Tables 1–3. Barotropic mode is by far the most energetic in all cases. In ES, it is more energetic in winter than in summer for constituents $M_2$ (above 85% of total energy in winter and 77% in summer), $S_2$ (87.5% in winter and ~73% in summer) and $O_1$ (above 78% in summer and ~70% in summer). $K_1$ is more energetic in summer (almost 80%) than in winter (around 70%).In CS (Table 3) the barotropic mode explains more than 93% for all constituents, a result previously reported by Candela et al. (1990), Mañanes et al. (1998) and Tsimplis (2000). The small fraction of energy not explained by the barotropic mode is accounted by the first baroclinic one for all constituents analysed except $M_2$. Both modes explain around 99% of the total energy. For $M_2$ constituent, modes 2 and 3 are more important than mode 1. The barotropic mode in ES explains a considerable less percentage of total energy, particularly in summer. For $M_2$ constituent, the second baroclinic mode is more important than the first one in winter and comparable to the first one during summer. Summer stratification favours a first-mode internal oscillation but also, and particularly, the third mode. It is not a surprising fact if we consider the vertical structure of amplitude in Fig. 4A with two well differentiated relative maxima in summer. The second shallower maximum is smoothed in winter and, consequently, the existence of a relevant third mode is not as necessary as in summer. The richer high mode structure in ES is thus consequence of the more complex vertical structure of the harmonic constants.

## 4. Summary and conclusions

The observations of the exchange at the two main sills of the Strait of Gibraltar (ES and CS) analysed in this work have evidenced the noticeable spatial variability of the tidal flow as well as some minor seasonal differences that follow from the separation of the one-year long series into smaller pieces spanning summer and winter seasons.

The mean (time averaged) flow structure illustrates the well-known deepening of the interface (the surface of null along-Strait velocity) when moving to the west.

Table 2
Amplitude $a_n$, phase $\theta_n$ and percentage of energy (inside parenthesis) for the barotropic mode and first five baroclinic modes normalised to Eq. (7) over ES during winter time

| | Constituent | | | |
|---|---|---|---|---|
| | $M_2$ | $S_2$ | $O_1$ | $K_1$ |
| Barotropic | 7.0, 149 (86.6) | 3.1, 188 (87.5) | 2.2, 28 (78.2) | 2.1, 101 (71.1) |
| Baroclinic 1 | 1.0, 135 (1.7) | 0.5, 141 (2.0) | 0.1, −46 (0.2) | 0.5, 236 (3.8) |
| Baroclinic 2 | 2.2, 203 (8.4) | 0.9, 223 (7.1) | 1.0, 62 (16.1) | 0.8, 159 (10.1) |
| Baroclinic 3 | 0.6, 156 (0.7) | 0.1, 160 (0.06) | 0.4, 74 (2.8) | 0.6, 194 (7.1) |
| Baroclinic 4 | 0.9, 152 (1.5) | 0.4, 171 (1.6) | 0.4, 18 (2.1) | 0.3, 198 (1.9) |
| Baroclinic 5 | 0.2, 177 (0.09) | 0.2, 228 (0.3) | 0.02, 69 (0.07) | 0.5, 226 (3.8) |

Table 3
Amplitude $a_n$, phase $\theta_n$ and percentage of energy (inside parenthesis) for the barotropic mode and first five baroclinic modes normalised to Eq. (7) over CS during winter time

| | Constituent | | | |
|---|---|---|---|---|
| | $M_2$ | $S_2$ | $O_1$ | $K_1$ |
| Barotropic | 15.9, 156 (97) | 6.3, 163 (94.1) | 4.1, 31 (93.2) | 2.7, 90 (93.3) |
| Baroclinic 1 | 1.1, 181 (0.4) | 1.4, 204 (4.6) | 1.0, −34 (5.9) | 0.5, 15 (3.9) |
| Baroclinic 2 | 1.5, 199 (0.9) | 0.6, 204 (1.0) | 0.2, 5 (0.2) | 0.3, 45 (1.1) |
| Baroclinic 3 | 1.6, 200 (1.0) | 0.3, 197 (0.3) | 0.2, 36 (0.2) | 0.3, 65 (0.8) |
| Baroclinic 4 | 1.1, 192 (0.4) | 0.2, 201 (0.05) | 0.1, −75 (0.09) | 0.2, −85 (0.35) |
| Baroclinic 5 | 0.6, 194 (0.1) | 0.01, 138 (0.003) | 0.1, −66 (0.07) | 0.1, −54 (0.1) |

In ES, the interface is around 40 m deeper than in CS. The outflowing velocity is greater in ES, where it shows a local maximum at around 100 m below the interface, which is greater and deeper in winter. During this season, the interface is also slightly shallower giving rise to an increased outflow in winter, a fact pointed out by García-Lafuente et al. (2007).

Over ES, only slight variations between winter and summer periods are observed for $M_2$ tidal current, especially through the interface layer. For $S_2$ and $K_1$ discrepancies between both periods are clearly evident. Amplitude in CS reaches maximum at a shallower depth than in ES and its value is higher for all tidal constituents (more than twice for $M_2$). Phases of diurnal constituents near the bottom are delayed with regards to phases near the surface, in contrast to what happened to the semidiurnal constituents.

DMD has been carried out to separate tidal velocities into barotropic and baroclinic components and relative importance of each mode has been determined in terms of the energy associated. For ES, barotropic mode is more energetic during wintertime for $M_2$, $S_2$ and $O_1$ constituents, $K_1$ being more energetic during summertime. In any case, total energy of barotropic mode is always above 70% (above 85% for semidiurnal constituents in winter) and baroclinic modes have smaller contributions. During wintertime, second baroclinic mode is more energetic than the first one and relatively high percentage of energy is accounted by third baroclinic mode for $M_2$ (8%) and $O_1$ (9%) constituents. Over CS, barotropic mode accounts for

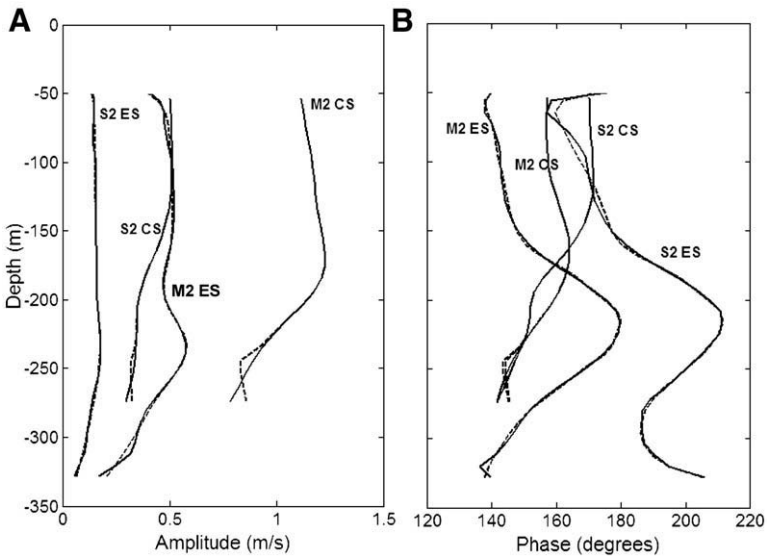


Fig. 10. Reproduction of amplitude (panel A) and phase (panel B) profiles of the semidiurnal tidal constituents (dashed line) from the combination of the barotropic and the first five baroclinic modes (normalised to Eq. (7)). For comparison purposes, the real profiles have also been displayed (solid line). ES and CS labelled beside each tidal constituent stand for Espartel and Camarinal sill, respectively. ES data corresponds to summertime and CS data to wintertime. No significant seasonal variations are observed in the fitting quality.

more than 90% of total energy in all the tidal constituents, the highest value (97%) observed for $M_2$.

## Acknowledgements

This work has been supported by the Spanish-funded INGRES projects (REN 2003-01608 and CTM2006-02326). We thank Prof. John Klink for his valuable commentaries on the DMD technique. We are also indebted to the crew of BO Odón de Buen for his work during INGRES surveys. A.S-R acknowledges a FPI grant from the Spanish Ministry of Science and Technology (ref. no. BES-2004-5530) and J.C.S a grant from the Consejería de Innovación, Ciencia y Empresa (Junta de Andalucía, Project RNM 968). Julio Candela is also acknowledged for the dissemination of CS data.

## References

Armi, L., Farmer, D.M., 1988. The flow of Mediterranean water through the Strait of Gibraltar. Progress in Oceanography 21, 1–105.

Baschek, B., Send, U., García Lafuente, J., Candela, J., 2001. Transport estimates in the Strait of Gibraltar with a tidal inverse model. Journal of Geophysical Research 106, 31033–31044.

Birkhoff, G., Rota, G.C., 1962. Ordinary Differential Equations. Ginn, Boston, Massachusetts.

Bruno, M., Mañanes, R., Alonso, J.J., Izquierdo, A., Tejedor, L., Kagan, B., 2000. Vertical structure of the semidiurnal tidal currents at Camarinal Sill, the Strait of Gibraltar. Oceanologica Acta 23, 15–24.

Bruno, M., Alonso, J.J., Cózar, A., Vidal, J., Echevarría, F., Ruiz, J., Ruiz-Cañavate, A., Gómez, F., 2002. The boiling water phenomena at Camarinal Sill, the Strait of Gibraltar. Deep-Sea Research II 49 (19), 4097–4113.

Bryden, H.L., Candela, J., Kinder, T.H., 1994. Exchange through the Strait of Gibraltar. Oceanologica Acta 33, 201–248.

Candela, J., Winant, C., Bryden, H.L., 1989. Meteorologically forced subinertial flows through the Strait of Gibraltar. Journal of Geophysical Research 94, 12667–12674.

Candela, J., Winant, C., Ruiz, A., 1990. Tides in the Strait of Gibraltar. Progress in Oceanography 33, 7313–7335.

Foreman, M.G.G., 1978, revised 2004. Manual for tidal currents analysis and prediction. Pacific Marine Science Report, 78–6. Institute of Ocean Sciences, Patricia Bay. 57 pp.

García Lafuente, J., Almazán, J.L., Castillejo, F., Khribeche, A., Hakimi, A., 1990. Sea level in the Strait of Gibraltar: Tides. International Hydrographic Review 47, 111–130.

García Lafuente, J., Vargas, J.M., Plaza, F., Sarhan, T., Candela, J., Baschek, B., 2000. Tide at the eastern section of the Strait of Gibraltar. Journal of Geophysical Research, 105, 14197–14213.

García Lafuente, J., Delgado, J., Vargas, J.M., Vargas, M., Plaza, F., Sarhan, T., 2002a. Low frequency variability of the exchanged flows through the Strait of Gibraltar during CANIGO. Deep-Sea Research II 49, 4051–4067.

García Lafuente, J., Delgado, J., Criado, F., 2002b. Inflow interruption by meteorological forcing in the Strait of Gibraltar. Geophysical Research Letters 29 (19), 1914. doi:10.1029/2002GL015446.

García-Lafuente, J., Sánchez-Román, A., Díaz del Río, G., Sannino, G., Sánchez Garrido, J.C., 2007. Recent observations of the seasonal variability of the Mediterranean outflow in the Strait of Gibraltar. Journal of Geophysical Research 112, C10005. doi: 10.1029/2006JC003992.

Garrett, C., Bormans, M., Thompson, K., 1990. Is the exchange through the Strait of Gibraltar maximal or submaximal? In: Pratt, L.J. (Ed.), The Physical Oceanography of Sea Straits. Kluwer Academic Publisher, Dordrecht, pp. 271–294.

Gill, A.E., 1982. Atmosphere–Ocean Dynamics. Academic Press, San Diego, California. 662 pp.

Kundu, P.K., Allen, J.S., Smith, R.L., 1975. Modal decomposition of the velocity field near the Oregon coast. Journal of Physical Oceanography 5, 638–704.

Lacombe, H., Richez, C., 1982. Regime of the Strait of Gibraltar and of its east and west approaches. In: Nihoul, J.C.J. (Ed.), Hydrodynamics of Semi-enclosed Seas. Elsevier-Sci., New York, pp. 13–73.

Mañanes, R., Bruno, M., Alonso, J., Fraguela, B., Tejedor, L., 1998. The nonlinear interaction between tidal and subinertial flows in the Strait of Gibraltar. Oceanologica Acta 21, 33–46.

Marchuk, G.I., Kagan, B.A., 1970. Internal gravitational waves in a really stratified ocean. Izvestiya Akad Nauk SSSR. Atmospheric and Oceanic Physics 6, 412–422.

Müller, T.J., Siedler, G., 1992. Multi-year current time series in the eastern North Atlantic Ocean. Journal of Marine Research 50, 63–98.

Pawlowicz, R., Beardsley, B., Lentz, S., 2002. Classical tidal harmonic analysis including error estimates in MATLAB using T_TIDE. Computers and Geosciences 28 (8), 929–937.

Reid, J.L., 1979. On the contribution of the Mediterranean Sea outflow to the Norwegian–Greenland Sea. Deep Sea Research, Part A, 26, 1199–1223 Vol. 28, N 8, 929–937.

Richez, C., 1994. Airborne synthetic aperture radar tracking of internal waves in the Strait of Gibraltar. Progress in Oceanography 33, 93–159.

Sannino, G., Bargagli, A., Artale, V., 2002. Numerical modelling of the mean exchange through the Strait of Gibraltar. Journal of Geophysical Research 179 (C08), 3094. doi:10.1029/2001JC000929.

Sannino, G., Bargagli, A., Artale, V., 2004. Numerical modelling of the semidiurnal tidal exchange through the Strait of Gibraltar. Journal of Geophysical Research 109, C05011. doi:10.1029/2003JC002057.

Schott, F., 1977. On the energetics of baroclinic tides in the North Atlantic. Annals of Geophysics 33, 41–62.

Siedler, G., Paul, U., 1991. Barotropic and baroclinic tidal currents in the eastern basins of the North Atlantic. Journal of Geophysical Research 96, 22259–22271.

Tsimplis, M.N., 2000. Vertical structure of the tidal currents over the Camarinal Sill at the Strait of Gibraltar. Journal of Geophysical Research 104, 13541–13557.

Tsimplis, M.N., Bryden, H.L., 2000. Estimation of the transport through the Strait of Gibraltar. Deep Sea Research, 47, 2219–2242 Part I.

Wang, D.P., 1993. The strait of Gibraltar model: internal tide, diurnal inequality and fortnightly modulations. Deep Sea Research 40, 1187–1203 Part I.